ARTICLES
https://doi.org/10.1038/s41563-021-00958-9

nature materials

Microstructural origin of locally enhanced CO_2 electroreduction activity on gold

Ruperto G. Mariano[1,3], Minkyung Kang[2,3], Oluwasegun J. Wahab[2], Ian J. McPherson[2], Joshua A. Rabinowitz[1], Patrick R. Unwin[2]✉ and Matthew W. Kanan[1]✉

Understanding how the bulk structure of a material affects catalysis on its surface is critical to the development of actionable catalyst design principles. Bulk defects have been shown to affect electrocatalytic materials that are important for energy conversion systems, but the structural origins of these effects have not been fully elucidated. Here we use a combination of high-resolution scanning electrochemical cell microscopy and electron backscatter diffraction to visualize the potential-dependent electrocatalytic carbon dioxide (CO_2) electroreduction and hydrogen (H_2) evolution activity on Au electrodes and probe the effects of bulk defects. Comparing colocated activity maps and videos to the underlying microstructure and lattice deformation supports a model in which CO_2 electroreduction is selectively enhanced by surface-terminating dislocations, which can accumulate at grain boundaries and slip bands. Our results suggest that the deliberate introduction of dislocations into materials is a promising strategy for improving catalytic properties.

Bulk defects are appealing design targets for heterogeneous catalysis because they are stable under many catalytically relevant conditions[1–8] and they can create substantial perturbations when they intersect with the surface[9–16]. The ability to utilize defects to improve catalysts hinges on establishing specific defect–activity relationships and, ultimately, understanding how these relationships manifest in surface structures. CO_2 electroreduction is an important testing ground for catalyst design elements because it is a major source of energy loss in many strategies to convert renewable energy to carbon-based fuels[17]. Au materials are the most active and selective known catalysts for CO_2 electroreduction to CO and therefore provide a useful model system to investigate the impact of defects on state-of-the-art activity[18].

The combination of electron backscatter diffraction (EBSD) and scanning electrochemical cell microscopy (SECCM) is a compelling strategy to directly correlate surface grain structure and electrocatalytic activity on polycrystalline electrodes[19–21]. EBSD creates a grain map that details the microstructure of a polycrystalline material, while SECCM provides spatially resolved current–potential measurements, which can be presented as maps, videos and nanoscale voltammograms, to reveal how activity depends on local microstructure[22]. We previously used EBSD and SECCM to study the CO_2 electroreduction and H_2 evolution reactions across grain boundaries (GBs) on Au electrodes[3]. This study showed that GBs can support micrometre-wide catalytic 'footprints' on Au, where CO_2 electroreduction is enhanced while H_2 evolution is not. However, it remained unclear whether the physical origin of this enhancement was locally altered lattice strain in the vicinity of the GBs or a local increase in undercoordinated site density.

Here, we employ high-resolution SECCM (diameter of droplet ≈ 200 nm) with environmental control[23] to produce spatially resolved electrochemical videos of CO_2 electroreduction and H_2 evolution in the vicinity of GBs. We find that H_2 evolution is largely insensitive to microstructure for the samples studied here, while CO_2 electroreduction shows a pronounced microstructure dependence. Using high-resolution EBSD (HR-EBSD), we show that regions of enhanced CO_2 electroreduction activity are not correlated with lattice strain but instead map directly onto sites with high geometrically necessary dislocation (GND) content induced by lattice rotation gradients. These findings support a model in which dislocations enhance CO_2 electroreduction by creating permanent steps at the electrode surface, which increases the density of undercoordinated sites. The accumulation of dislocations in the vicinity of the GB is the likely origin of GB-localized enhancements observed previously, but dislocations can also accumulate at other features such as slip bands (SBs).

Experimental set-up for SECCM

SECCM uses a mobile, nanoscale electrochemical half-cell composed of a nanopipette (tip diameter ≈ 200 nm; Supplementary Fig. 1a). The nanopipette is filled with electrolyte, forming a nanodroplet with a diameter approximately equal to the tip aperture (Fig. 1), and equipped with a quasi-reference counter electrode (QRCE, an Ag/AgCl wire) distal to the tip[24,25]. In SECCM, the nanodroplet (rather than the nanopipette itself) makes contact with the surface of interest. Thus, when a potential is applied between the surface and the QRCE, the electrochemical current is measured only from the surface area contacted by the nanodroplet[26]. An SECCM scan is composed of an array of 'hops' with sub-micrometre spacing over a targeted area, using the current that flowed upon meniscus contact as feedback to control tip movement (Supplementary Fig. 1). A linear sweep voltammogram (LSV) is collected at each hop, and the resulting dataset comprises a series of equipotential electrochemical images, constituting an electrochemical video with ~750 frames[27]. The tip position is recorded synchronously, also allowing the construction of a colocated topography map (Fig. 1b).

The choice of electrolyte is important for maintaining a uniform meniscus contact size in an SECCM scan. We found that 10 mM sodium citrate, pH 5.5, yielded stable droplets over timescales that permitted SECCM scans comprising >1,000 points. To understand mass-transport rates in the SECCM configuration, we performed finite element method calculations (Supplementary Note 1). Under

[1]Department of Chemistry, Stanford University, Stanford, CA, USA. [2]Department of Chemistry, University of Warwick, Coventry, UK. [3]These authors contributed equally: Ruperto G. Mariano, Minkyung Kang. ✉e-mail: P.R.Unwin@warwick.ac.uk; mkanan@stanford.edu

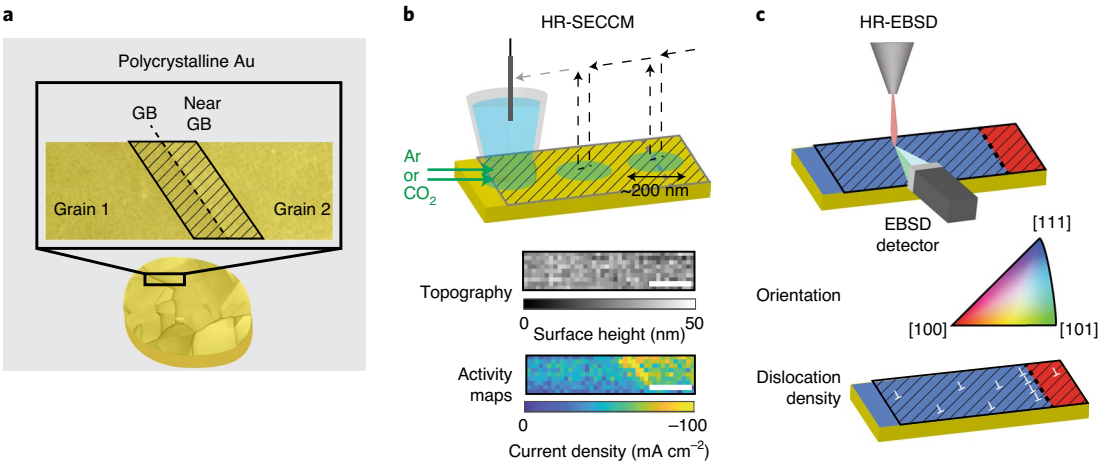

Fig. 1 | Experimental approach for investigating microstructure effects in electrocatalysis at Au electrodes. a, Cartoon of the regions of interest probed by correlative SECCM and HR-EBSD measurements. **b**, Illustration of voltammetric SECCM deployed in a hopping mode (dashed arrows) on a polycrystalline Au surface under environmental control. The SECCM probe is brought into meniscus contact with the Au substrate at a series of points (image pixels), and a voltammogram is measured at each point, simultaneously generating a topography map and activity maps. Scale bars in the maps are 5 µm. **c**, Schematic of HR-EBSD grain mapping in a colocated region of the Au electrode, performed after SECCM experiments. The blue and red surfaces correspond to two grains with different orientations indicated by the inverse pole figure legend. The dislocation density schematic shows a variation in dislocation density across the grain surfaces, including a high-density region next to the GB.

an Ar atmosphere, H_2 evolution is the only possible cathodic reaction in this electrolyte; the mass-transport-limited current density for H_2 evolution with H_3O^+ and citric acid as the proton donors is ~60 mA cm^{-2} (Supplementary Note 1 and Supplementary Fig. 2b,c). The participation of H_2O as a proton donor removes this limit. Under a CO_2 atmosphere, a very high mass-transport limit of 58 A cm^{-2} for CO_2 electroreduction is obtained, which reflects the rapid diffusion of CO_2 through the nanodroplet to the electrode surface (Supplementary Fig. 2a).

Product distributions cannot be quantified in SECCM measurements because the absolute currents are very low (<1 nA). We therefore independently evaluated a Au catalyst in citrate electrolyte using a gas diffusion electrode to mimic the CO_2 transport properties of SECCM (Methods)[28]. Under CO_2 atmosphere, the faradaic efficiency for CO_2 electroreduction to CO was essentially quantitative from −0.9 to −1.1 V versus Ag/AgCl (Supplementary Figs. 3 and 4). Although the architecture of the catalyst layer in the gas diffusion electrode may enhance citrate and pH gradients that contribute to suppressing H_2 evolution, these results indicate that CO_2 reduction is the dominant reaction in this electrolyte within the potential range studied here. Prior studies at similar potentials have shown that CO_2 reduction to CO is independent of pH across a broad pH range and proceeds with near-unity selectivity in poorly buffering electrolytes[29–34].

The substrates used during SECCM mapping were prepared by pressing small polycrystalline Au nuggets against a flat Si surface prior to annealing at 900 °C. This procedure resulted in a surface with large grains (>100 µm) and GBs visible to an optical camera, allowing for positioning of the nanopipette in the vicinity of GBs. The samples were imaged by EBSD to provide a grain orientation map, from which the regions for SECCM mapping were selected (Fig. 1c).

High-resolution electrochemical mapping of H_2 evolution and CO_2 electroreduction

To probe the effects of surface microstructure on H_2 evolution and CO_2 electroreduction, we first performed a set of SECCM scans under Ar and CO_2 atmospheres, respectively, using the same sample (designated as Sample A). Figure 2 shows the results of a scan under Ar. The scanned region contained one low-angle GB (GB1, with a misorientation of 4°) that bisected two grains with a *z*-direction orientation close to the [101] direction (Grains B and C; precise Euler angles for all grains studied are detailed in Supplementary Table 1), and a high-angle GB (GB2, with a misorientation of 42°) that bisected Grain B and a grain with a *z*-direction orientation close to the [111] direction (Grain A, Fig. 2a). Using a 0.7 µm step size, we collected a 49 µm × 7.7 µm SECCM map (770 points). Scanning electron microscopy (SEM) imaging after SECCM allowed us to observe the footprint of electrolyte residue left behind by each meniscus contact (dark features in Fig. 2c), the size of which (~200 nm) was approximately equal to the tip aperture. The topographical map obtained from the SECCM scans (from the nanopipette *z* position at each meniscus contact) indicated an elevated region in Grain A, adjacent to GB2 (Fig. 2e). The electrolyte footprint was consistent across the entire scan range, even as the nanopipette traversed the topographical feature and crossed the GBs, which indicates that the size of each region of contact (electrochemical cell) was consistent throughout the scan.

Each pixel in the SECCM map is a LSV from −0.30 to −1.05 V. The combination of all the LSVs is an electrochemical 'video' showing the spatial distribution of activity as a function of potential (Supplementary Video 1). A snapshot at −1.05 V is shown in Fig. 2d. To quantify the current distribution, we subdivided the SECCM map into six regions corresponding to the individual grains, GBs and topographical features (Fig. 2e) and extracted histograms of the current densities in each region at selected potentials (Fig. 2f). The H_2 evolution activity was slightly lower in Grain A (62 ± 2 mA cm^{-2} at −1.05 V) compared to Grain B (65 ± 5 mA cm^{-2} at −1.05 V; Fig. 2f). No enhancement in current was observed around either GB1 or GB2 (which have very different GB angles), compared to their adjacent regions, which indicates that H_2 evolution is not dependent on local defect structure on Au. This observation is consistent with recent electrochemical studies of H_2 evolution on Au single crystals[35].

In contrast to H_2 evolution, SECCM under CO_2 revealed microstructural sensitivity. Figure 3 shows the results of a 30.5 µm × 9.5 µm SECCM scan with 0.5 µm spacing (1,159 points). Viewed along the *z* direction, the scanned region contained two grains oriented close to

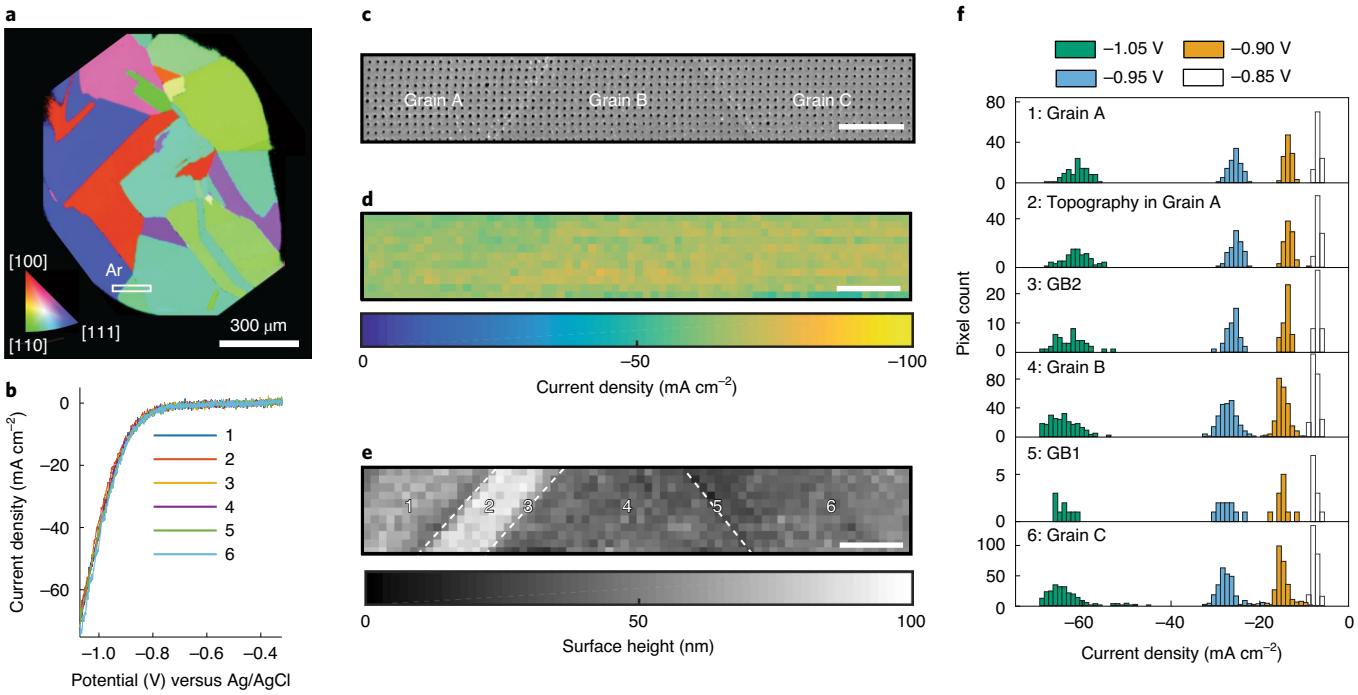

Fig. 2 | Probing microstructure dependence of H_2 evolution activity. a, EBSD orientation map of Sample A viewed along the *z* direction. White rectangle indicates the location of the SECCM scan. Inverse pole figure legend for EBSD orientations is inset. **b**, LSVs extracted from individual pixels in the six regions indicated in **e**. **c**, SEM map of the region scanned with SECCM, showing residues left from droplet contact points. **d**, Snapshot of the SECCM video at −1.05 V versus Ag/AgCl. **e**, Topographic map of the scanned region. Inset numbers indicate the origin of pixels used to build the histogram in **f**. **f**, Histograms of current densities from all of the pixels in each region marked in **e**. For assignment of pixels to each region, see Supplementary Fig. 6a. The scale bars in **c**, **d** and **e** are 5 µm.

the [111] (Grain A) and [100] (Grain D) directions joined by a Σ3 GB (Fig. 3a and Supplementary Table 1). SEM imaging performed after the SECCM scans showed consistent electrolyte footprints of ~200 nm diameter (Fig. 3c), with no systematic variation observed across the grains or the GB. No prominent features were evident in the topographical map (Fig. 3e). As seen in Supplementary Video 2 and in the snapshot taken at –1.05 V (Fig. 3d), Grain A exhibited higher activity than Grain D. In addition, the highest activity was obtained in a feature 1 to 3 pixels wide (0.5–1.5 µm) within Grain A that runs parallel to the Σ3 GB, along a $<1\bar{1}0>$ direction. This alignment suggests that the parallel feature is a SB, which is generated by the migration of dislocations in Au{111} planes (Supplementary Fig. 5)[36]. The SB is also evident in the SEM image in Fig. 3c.

The current distribution in the two grains and the SB was quantitatively compared by analysing all of the pixels in these three regions. The pixels corresponding to the SB were extracted from the region of 1 to 3 pixel width that corresponds to the feature in the SEM image (marked SB, Fig. 3c). Figure 3b shows an overlay of LSVs from three representative pixels residing in the two grains and the SB, while Fig. 3f shows histograms of the currents in all of the pixels of each region at selected potentials. The largest differences were observed at −1.05 V, where the average current densities were 74 ± 4 mA cm^{-2} for Grain D, 84 ± 5 mA cm^{-2} for Grain A and 94 ± 5 mA cm^{-2} for the SB. The top 10% of the most active pixels in the SB and Grain A exhibited currents of at least 100 mA cm^{-2} and 90 mA cm^{-2}, respectively.

A second pair of SECCM scans of Sample A under Ar and CO_2 was obtained over regions contained within Grain C. The grain contained a prominent topographical feature. For both the Ar and CO_2 scans, the resulting electrochemical map at −1.05 V versus Ag/AgCl showed very homogeneous activity throughout the entire scanned region (Supplementary Figs. 7 and 8 and Supplementary Videos 3 and 4). Together, the four SECCM scans of Sample A demonstrate that H_2 evolution has essentially no structural dependence, while CO_2 electroreduction depends on grain orientation and the presence of a defect such as a SB. This dependence does not arise from topography as the current shows no dependence on topography under either Ar or CO_2.

Structural origin of enhanced activity at the SB

To investigate how the SB enhanced CO_2 electroreduction catalysis, we employed HR-EBSD to map the deformation around the Σ3 GB region at a resolution of ~170 nm. HR-EBSD enables measurement of both strain and lattice rotations by cross-correlating subpixel shifts in the diffraction patterns at each pixel to a reference pixel distal from highly deformed regions[37–40], and has been previously used to measure strain and lattice rotation in a variety of materials[41–45]. The lattice rotations in the vicinity of the Σ3 GB of Sample A were found to be less than ~0.2°, which permitted the analysis of the HR-EBSD data without additional remapping corrections (Supplementary Fig. 9)[37,46].

We first investigated the role of lattice strain on electrocatalytic activity. The normal strains in the x (ε_{11}), y (ε_{22}) and z (ε_{33}) directions were calculated from the HR-EBSD data to construct strain maps (Fig. 4a–c). The SB region exhibited an inversion of the ε_{11} and ε_{22} strains, supporting the assignment of this feature as a SB and indicating the presence of dislocations[47–49]. If strain is predictive of electrocatalytic activity, the SECCM current should exhibit spatial variations corresponding to the local lattice strain. However, there was no correlation between electrochemical activity (Fig. 4d) and any of the normal strains.

Figure 4e shows a map of the lattice rotation gradients obtained from the HR-EBSD data. We observed large lattice rotation gradients in a continuous line within the SB region, which indicates the presence

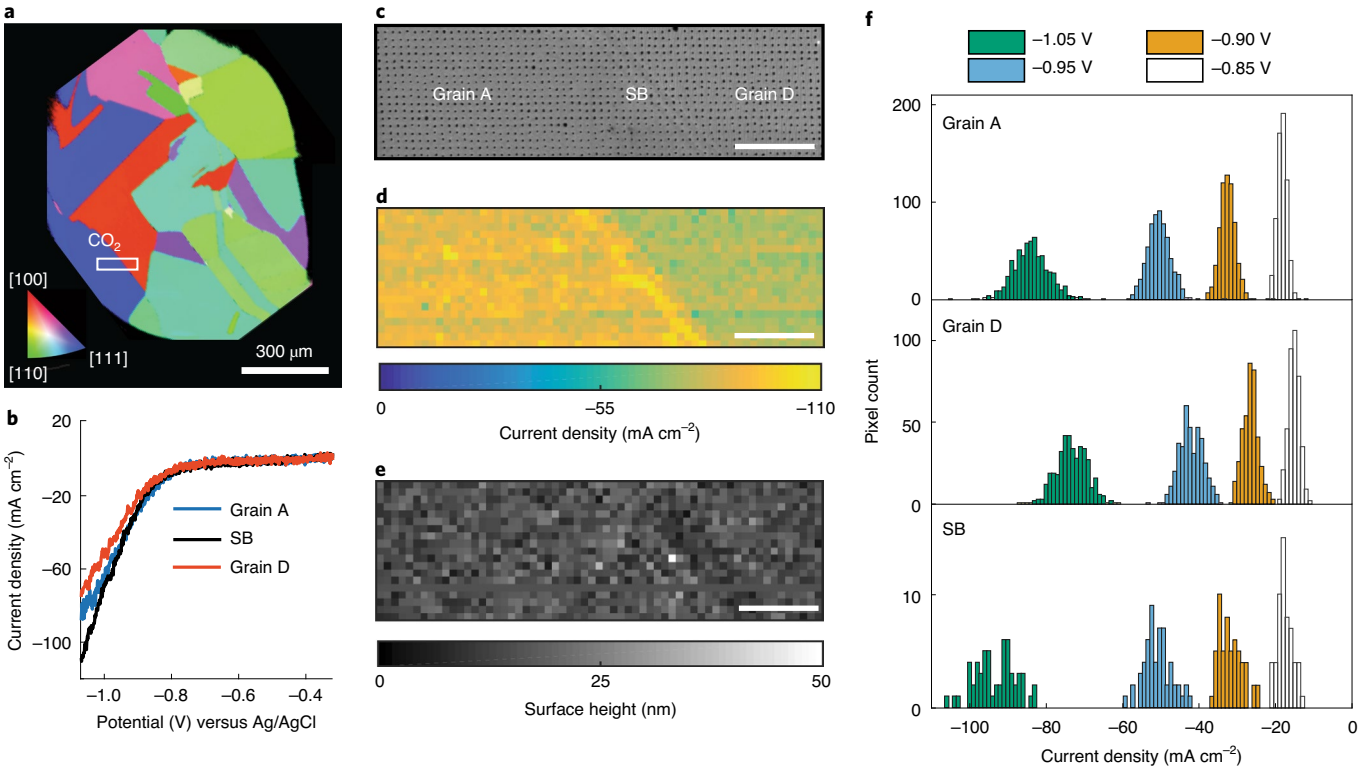

Fig. 3 | Probing microstructure dependence of CO_2 electroreduction activity. a, EBSD orientation map of Sample A viewed along the *z* direction. White rectangle indicates the location of the SECCM scan in CO_2 atmosphere. Inverse pole figure legend for EBSD orientations is inset. **b**, LSVs extracted from individual pixels in the three regions in **c**. **c**, SEM image of the scanned region after SECCM mapping. Inset text indicates the regions from which pixels for the histogram in **f** were extracted. **d**, Snapshot of the SECCM video at −1.05 V versus Ag/AgCl. **e**, Topographic map of the regions probed with SECCM. **f**, Histograms of current densities from all of the pixels in each region marked in **c**. For assignment of pixels to each region, see Supplementary Fig. 6b. The scale bars in **c**, **d** and **e** are 5 μm.

of lattice curvature and GNDs to accommodate such curvature (Supplementary Fig. 10)[36]. The lattice rotation gradients can be used to compute a lower-bound estimate of the GND density (ρ_{GND}) as described in detail elsewhere[37,38,41,43,44,49,50]. We found a large ρ_{GND} (~30–50 μm^{-2}) in a continuous line in the SB region coinciding with the large rotation gradients (Fig. 4f). While the observed ρ_{GND} corresponded to a volume fraction of less than 0.001% (Supplementary Note 2), these minority features can have an outsized influence on the surface structure. Several high-resolution scanning tunnelling microscopy studies have shown that surface-terminating dislocations nucleate ~0.1-μm-long to 1-μm-long atomic step ridges observed on Au(111) single crystals[9,12,13]. The ~10 mA cm^{-2} difference in current density at −1.05 V observed between the SB and Grain A could be explained by a higher coverage of highly active undercoordinated sites[35] in the SB region arising from these dislocation-associated steps. For example, if the dislocation-associated sites were operating at 10% of the SECCM mass-transport limit (5.8 A cm^{-2}), a ~0.17% coverage would be required to account for 10 mA cm^{-2}. If at least half of the observed GNDs terminate on the surface (~25 μm^{-2}), this coverage corresponds to an average ~70 nm^2 footprint of highly active sites associated with each dislocation-associated step ridge.

SECCM across a GB in a defect-rich sample

A second sample (Sample B) was prepared in the same way as Sample A except that it was pressed against the Si substrate with greater pressure using a vice prior to annealing at 900 °C in order to generate more bulk defects. EBSD mapping indicated large orientation gradients within the individual grains of Sample B, which indicates residual deformation (Supplementary Fig. 11a). A two-grain region composed of one grain oriented 5.7° from the [101] direction (Grain E) and another grain oriented 13.6° from the [100] direction (Grain F) bisected by a 42° GB was selected for SECCM mapping (Fig. 5a; orientations in Supplementary Table 1 and Supplementary Fig. 11d). Orientation line profiles extracted from the EBSD maps indicated large misorientations of up to 4° within Grain E, and smaller, but still substantial, misorientations of up to 1° within Grain F (Fig. 5b). By comparison, misorientations in the vicinity of the Σ3 GB in Sample A were less than ~0.2° (Supplementary Fig. 5c) and within the angular resolution of Hough-based EBSD indexing[51]. Because lattice curvature must be accommodated by dislocations[36], the results in Fig. 5b indicate that Sample B likely has a large ρ_{GND}. It is difficult to accurately quantify ρ_{GND} from HR-EBSD in this highly deformed sample without advanced remapping corrections[37,46], but the disparity in misorientation gradients implies that Sample B has a substantially larger ρ_{GND} than Sample A.

A 13.5 μm × 14 μm SECCM scan (756 points) under CO_2 was collected over the entire region in Fig. 5a, again with consistent electrolyte footprints (~200 nm diameter) throughout the scan (Supplementary Fig. 11c). As seen in Supplementary Video 5, the SECCM map showed three distinct regions with electrochemical activity in the order GB > Grain E > Grain F (Fig. 5c and Supplementary Video 5), which was not topography dependent (Supplementary Fig. 12c). The enhancement of activity at the GB was evident even at low driving forces (as early as −0.8 V in Supplementary Video 5). An analysis of all the pixels in the three regions at selected potentials is shown in Fig. 5e. At −1.05 V, the average current densities were −185 ± 21 mA cm^{-2} for Grain E, −156 ± 14 mA cm^{-2} for Grain F and −210 ± 24 mA cm^{-2} for the 42° GB,

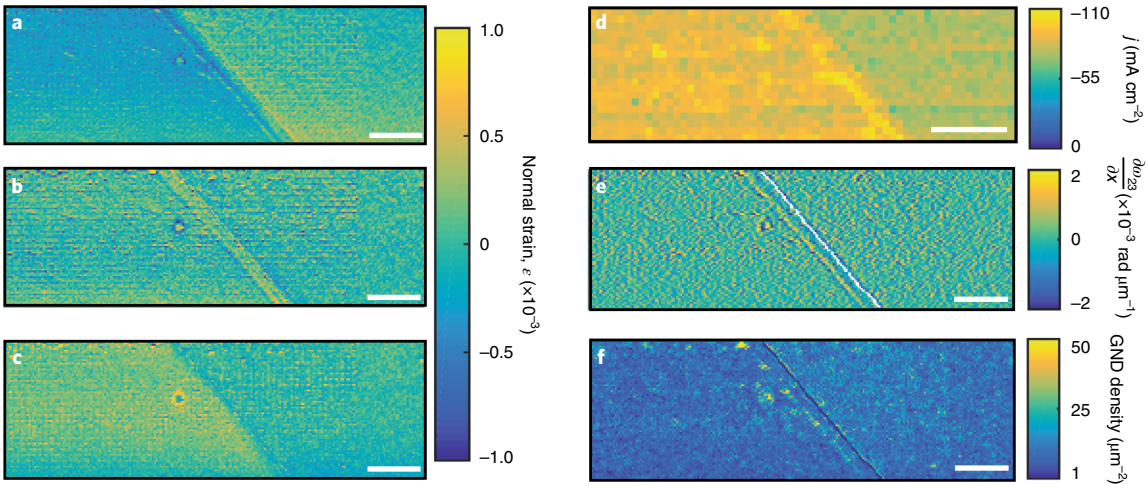

Fig. 4 | HR-EBSD mapping of area within Sample A that was scanned with SECCM, shown in Fig. 3. a, Normal strain profile in the *x* direction (ε_{11}). **b**, Normal strain profile in the *y* direction (ε_{22}). **c**, Normal strain profile in the *z* direction (ε_{33}). **d**, Snapshot of the SECCM video at −1.05 V versus Ag/AgCl reproduced from Fig. 3d. *j* is the current density. **e**, Lattice rotation gradient of the Σ3 GB ($\frac{\partial \omega_{23}}{\partial x}$). **f**, GND density map derived from the rotation gradients. Scale bars are 5 μm.

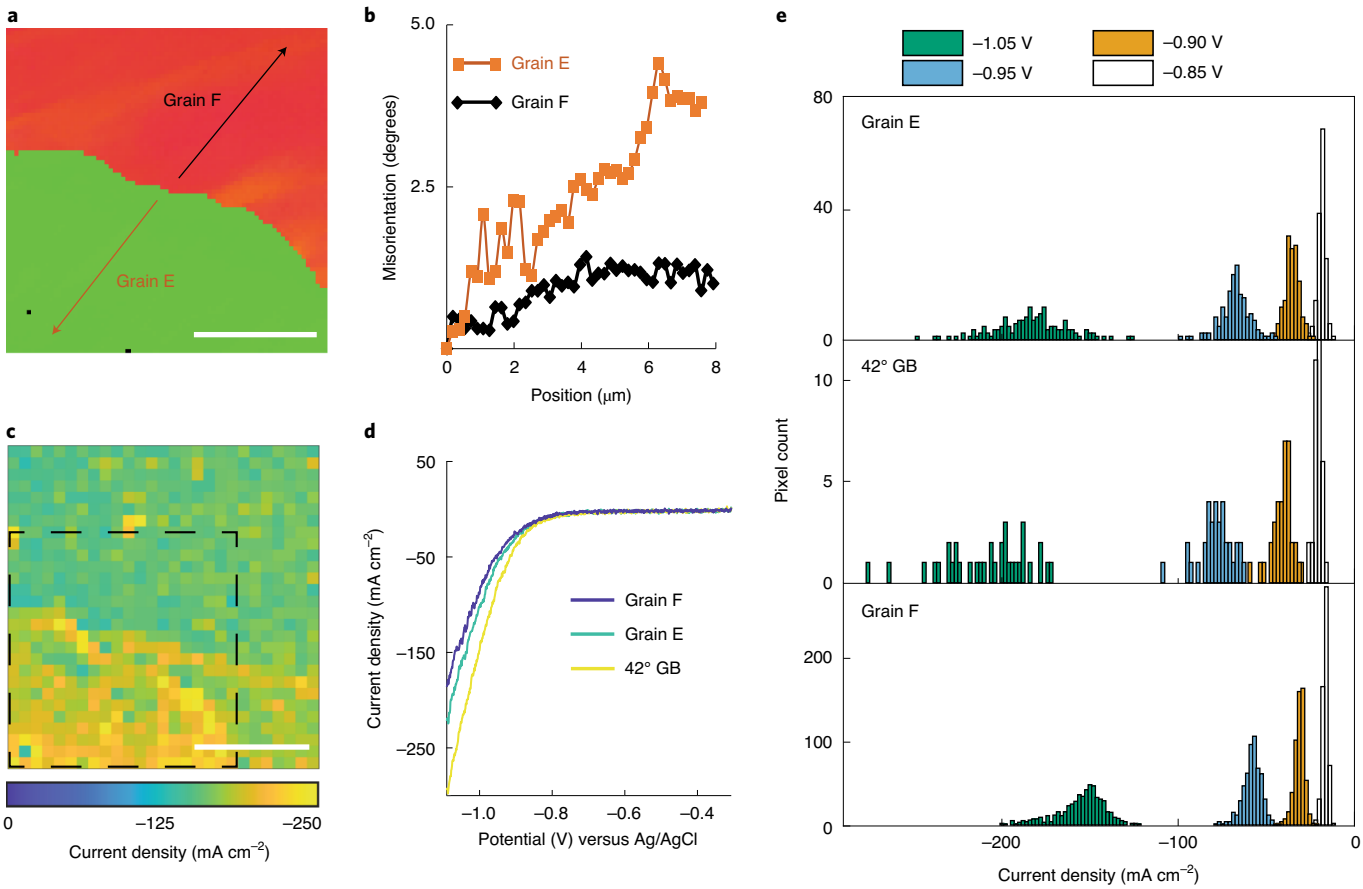

Fig. 5 | EBSD and SECCM mapping of a highly deformed region surrounding a 42° GB in Sample B. a, EBSD orientation map viewed along the *z* direction of a portion of the area probed by SECCM. Inset arrows indicate origin of misorientation line profiles shown in **b**. The two black pixels are unindexed pixels from the EBSD map. For an illustration of orientations, see Supplementary Fig. 11d. **b**, Hough-based misorientation line profiles along the lines indicated by arrows in **a**. **c**, Snapshot of the SECCM video at −1.05 V versus Ag/AgCl. Inset dashed box indicates origin of the EBSD map in **a**. **d**, LSVs extracted from individual pixels in the two grains and the GB region. **e**, Histograms of current densities from all of the pixels in each of the three regions. For assignment of pixels to each region, see Supplementary Fig. 6c. The scale bars in **a** and **c** are 5 μm.

corresponding to a ~15–37% increase at the GB site relative to the grains. The top 10% of the most active pixels in the GB and Grain E exhibited currents of at least $-245\,mA\,cm^{-2}$ and $-213\,mA\,cm^{-2}$, respectively.

The enhanced current density at the 42° GB in Sample B demonstrates that some GBs are highly active for CO_2 electrocatalysis, as we have observed previously[3]. We attribute this enhanced activity to increased step coverage on the surface in the 42° GB region, resulting from dislocations that accumulated in this region because their migration was blocked during the deformation and annealing process. It is important to note that since the dislocation 'pile up' depends on the sample history and GB character, the presence of a GB itself is not a guarantee of a high-ρ_{GND} region. The Σ3 GB of Sample A showed no increase in ρ_{GND} measured by HR-EBSD and no enhancement in current density for CO_2 electroreduction.

A broader comparison of the SECCM maps under CO_2 for Sample A and Sample B provides further insights into the microstructural sensitivity of CO_2 electroreduction on Au. Overall, the current densities observed for Sample B are ×1.5–2.5 larger than Sample A (compare with Figs. 3f and 5e and Supplementary Fig. 8j). Some, but not all, of this difference can be attributed to grain orientation. The most active grain, Grain E in Sample B, is oriented close to [101], which has previously been observed to have higher activity than other low index facets[35]. However, Grain F in Sample B exhibits mostly (100) character, which is a low-activity facet, yet it shows higher activity than all the regions (three grains, Σ3 GB and SB) probed under CO_2 in Sample A. In addition, the histograms in Fig. 5e versus Fig. 3f indicate a much wider spread of current densities in Sample B. The combination of higher overall activity and greater heterogeneity in the activity on Sample B reflects the heterogeneous deformation of the sample that is evident in the grain misorientations, further highlighting the contribution of dislocations to CO_2 electroreduction activity.

Our measurements have provided high-resolution, potential-dependent maps over relatively large areas of a Au electrode to enable a broad investigation of the role of defects and lattice deformation on CO_2 electroreduction. The results show that CO_2 electroreduction on Au is not sensitive to lattice strain per se. Instead, CO_2 electroreduction depends on dislocation density, which can be enhanced at GBs that have arrested dislocation migration or at other defects such as SBs. This phenomenon is attributed to the nucleation of steps at dislocation surface terminations, which change the population of undercoordinated sites that have been implicated as the most active sites for CO_2 electroreduction[35]. By contrast, H_2 evolution does not depend on undercoordinated sites, and shows no such enhancement in rate at these locations, providing further evidence for the structural basis for selective enhancement of CO_2 electroreduction. These studies provide a road map for understanding microscopic structure–activity relationships in electrocatalysis, and motivate the broader exploration of GB and dislocation engineering to improve the performance of electrocatalytic materials.

Online content

Any methods, additional references, Nature Research reporting summaries, source data, extended data, supplementary information, acknowledgements, peer review information; details of author contributions and competing interests; and statements of data and code availability are available at https://doi.org/10.1038/s41563-021-00958-9.

Received: 6 August 2020; Accepted: 11 February 2021;
Published online: 18 March 2021

References

1. Feng, X., Jiang, K., Fan, S. & Kanan, M. W. Grain-boundary-dependent CO_2 electroreduction activity. *J. Am. Chem. Soc.* **137**, 4606–4609 (2015).
2. Feng, X., Jiang, K., Fan, S. & Kanan, M. W. A direct grain-boundary-activity correlation for CO electroreduction on Cu nanoparticles. *ACS Cent. Sci.* **2**, 169–174 (2016).
3. Mariano, R. G., McKelvey, K., White, H. S. & Kanan, M. W. Selective increase in CO_2 electroreduction activity at grain-boundary surface terminations. *Science* **358**, 1187–1192 (2017).
4. Verdaguer-Casadevall, A. et al. Probing the active surface sites for CO reduction on oxide-derived copper electrocatalysts. *J. Am. Chem. Soc.* **137**, 9808–9811 (2015).
5. Lee, S. H. et al. Correlating oxidation state and surface area to activity from operando studies of copper CO electroreduction catalysts in a gas-fed device. *ACS Catal.* **10**, 8000–8011 (2020).
6. Xu, Z. et al. Dynamic restructuring induced Cu nanoparticles with ideal nanostructure for selective multi-carbon compounds production via carbon dioxide electroreduction. *J. Catal.* **383**, 42–50 (2020).
7. Humphreys, F. J. A unified theory of recovery, recrystallization and grain growth, based on the stability and growth of cellular microstructures—I. The basic model. *Acta Mater.* **45**, 4231–4240 (1997).
8. Humphreys, J., Rohrer, G. S. & Rollett, A. in *Recrystallization and Related Annealing Phenomena* 3rd edn, 145–197 (Elsevier, 2017).
9. Engbæk, J., Schiøtz, J., Dahl-Madsen, B. & Horch, S. Atomic structure of screw dislocations intersecting the Au(111) surface: a combined scanning tunneling microscopy and molecular dynamics study. *Phys. Rev. B* **74**, 195434 (2006).
10. Chidsey, C. E. D., Loiacono, D. N., Sleator, T. & Nakahara, S. STM study of the surface morphology of gold on mica. *Surf. Sci.* **200**, 45–66 (1988).
11. Radetic, T., Lançon, F. & Dahmen, U. Chevron defect at the intersection of grain boundaries with free surfaces in Au. *Phys. Rev. Lett.* **89**, 085502 (2002).
12. Giela, T., Freindl, K., Spiridis, N. & Korecki, J. Au(111) films on W(110) studied by STM and LEED – uniaxial reconstruction, dislocations and Ag nanostructures. *Appl. Surf. Sci.* **312**, 91–96 (2014).
13. Morgenstern, K., Lægsgaard, E. & Besenbacher, F. STM study of step dynamics around a bulk dislocation intersection with a Ag(111) surface. *Phys. Rev. B* **71**, 155426 (2005).
14. Christiansen, J. et al. Atomic-scale structure of dislocations revealed by scanning tunneling microscopy and molecular dynamics. *Phys. Rev. Lett.* **88**, 206106 (2002).
15. Barth, J. V., Brune, H., Ertl, G. & Behm, R. J. Scanning tunneling microscopy observations on the reconstructed Au(111) surface: atomic structure, long-range superstructure, rotational domains, and surface defects. *Phys. Rev. B* **42**, 9307–9318 (1990).
16. Trevor, D. J., Chidsey, C. E. D. & Loiacono, D. N. In situ scanning-tunneling-microscope observation of roughening, annealing, and dissolution of gold (111) in an electrochemical cell. *Phys. Rev. Lett.* **62**, 929–932 (1989).
17. Grim, R. G. et al. Transforming the carbon economy: challenges and opportunities in the convergence of low-cost electricity and reductive CO_2 utilization. *Energy Environ. Sci.* **13**, 472–494 (2020).
18. Hori, Y., Kikuchi, K. & Suzuki, S. Production of CO and CH_4 in electrochemical reduction of CO_2 at metal electrodes in aqueous hydrogencarbonate solution. *Chem. Lett.* **14**, 1695–1698 (1985).
19. Bentley, C. L., Kang, M. & Unwin, P. R. Nanoscale surface structure–activity in electrochemistry and electrocatalysis. *J. Am. Chem. Soc.* **141**, 2179–2193 (2019).
20. Aaronson, B. D. B. et al. Pseudo-single-crystal electrochemistry on polycrystalline electrodes: visualizing activity at grains and grain boundaries on platinum for the Fe^{2+}/Fe^{3+} redox reaction. *J. Am. Chem. Soc.* **135**, 3873–3880 (2013).
21. Wang, Y., Gordon, E. & Ren, H. Mapping the nucleation of H_2 bubbles on polycrystalline Pt via scanning electrochemical cell microscopy. *J. Phys. Chem. Lett.* **10**, 3887–3892 (2019).
22. Kang, M., Momotenko, D., Page, A., Perry, D. & Unwin, P. R. Frontiers in nanoscale electrochemical imaging: faster, multifunctional, and ultrasensitive. *Langmuir* **32**, 7993–8008 (2016).
23. Ornelas, I. M., Unwin, P. R. & Bentley, C. L. High-throughput correlative electrochemistry–microscopy at a transmission electron microscopy grid electrode. *Anal. Chem.* **91**, 14854–14859 (2019).
24. Bentley, C. L., Kang, M. & Unwin, P. R. Nanoscale structure dynamics within electrocatalytic materials. *J. Am. Chem. Soc.* **139**, 16813–16821 (2017).
25. Wahab, O. J., Kang, M. & Unwin, P. R. Scanning electrochemical cell microscopy: a natural technique for single entity electrochemistry. *Curr. Opin. Electrochem.* **22**, 120–128 (2020).
26. Ebejer, N. et al. Scanning electrochemical cell microscopy: a versatile technique for nanoscale electrochemistry and functional imaging. *Annu. Rev. Anal. Chem.* **6**, 329–351 (2013).
27. Bentley, C. L. et al. Electrochemical maps and movies of the hydrogen evolution reaction on natural crystals of molybdenite (MoS_2): basal *vs.* edge plane activity. *Chem. Sci.* **8**, 6583–6593 (2017).

28. Ripatti, D. S., Veltman, T. R. & Kanan, M. W. Carbon monoxide gas diffusion electrolysis that produces concentrated C_2 products with high single-pass conversion. *Joule* **3**, 240–256 (2019).
29. Ringe, S. et al. Double layer charging driven carbon dioxide adsorption limits the rate of electrochemical carbon dioxide reduction on gold. *Nat. Commun.* **11**, 33 (2020).
30. Wuttig, A., Yaguchi, M., Motobayashi, K., Osawa, M. & Surendranath, Y. Inhibited proton transfer enhances Au-catalyzed CO_2-to-fuels selectivity. *Proc. Natl Acad. Sci. USA* **113**, E4585–E4593 (2016).
31. Zhang, B. A., Ozel, T., Elias, J. S., Costentin, C. & Nocera, D. G. Interplay of homogeneous reactions, mass transport, and kinetics in determining selectivity of the reduction of CO_2 on gold electrodes. *ACS Cent. Sci.* **5**, 1097–1105 (2019).
32. Wuttig, A., Yoon, Y., Ryu, J. & Surendranath, Y. Bicarbonate is not a general acid in Au-catalyzed CO_2 electroreduction. *J. Am. Chem. Soc.* **139**, 17109–17113 (2017).
33. Ooka, H., Figueiredo, M. C. & Koper, M. T. M. Competition between hydrogen evolution and carbon dioxide reduction on copper electrodes in mildly acidic media. *Langmuir* **33**, 9307–9313 (2017).
34. Hall, A. S., Yoon, Y., Wuttig, A. & Surendranath, Y. Mesostructure-induced selectivity in CO_2 reduction catalysis. *J. Am. Chem. Soc.* **137**, 14834–14837 (2015).
35. Mezzavilla, S., Horch, S., Stephens, I. E. L., Seger, B. & Chorkendorff, I. Structure sensitivity in the electrocatalytic reduction of CO_2 with gold catalysts. *Angew. Chem. Int. Ed.* **131**, 3814–3818 (2019).
36. Cai, W. & Nix, W. D. *Imperfections in Crystalline Solids* (Cambridge Univ. Press, 2016).
37. Britton, T. B., Holton, I., Meaden, G. & Dingley, D. High angular resolution electron backscatter diffraction: measurement of strain in functional and structural materials. *Microsc. Anal.* **27**, 8–13 (2013).
38. Wilkinson, A. J. & Randman, D. Determination of elastic strain fields and geometrically necessary dislocation distributions near nanoindents using electron back scatter diffraction. *Phil. Mag.* **90**, 1159–1177 (2010).
39. Dingley, D. J., Wilkinson, A. J., Meaden, G. & Karamched, P. S. Elastic strain tensor measurement using electron backscatter diffraction in the SEM. *J. Electron Microsc.* **59**, S155–S163 (2010).
40. Wilkinson, A. J., Meaden, G. & Dingley, D. J. Mapping strains at the nanoscale using electron back scatter diffraction. *Superlattices Microstruct.* **45**, 285–294 (2009).
41. Jiang, J., Britton, T. B. & Wilkinson, A. J. Evolution of dislocation density distributions in copper during tensile deformation. *Acta Mater.* **61**, 7227–7239 (2013).
42. Guo, Y., Britton, T. B. & Wilkinson, A. J. Slip band–grain boundary interactions in commercial-purity titanium. *Acta Mater.* **76**, 1–12 (2014).
43. Littlewood, P. D., Britton, T. B. & Wilkinson, A. J. Geometrically necessary dislocation density distributions in Ti-6Al-4V deformed in tension. *Acta Mater.* **59**, 6489–6500 (2011).
44. Wallis, D., Hansen, L. N., Britton, T. B. & Wilkinson, A. J. Geometrically necessary dislocation densities in olivine obtained using high-angular resolution electron backscatter diffraction. *Ultramicroscopy* **168**, 34–45 (2016).
45. Britton, T. B., Liang, H., Dunne, F. P. E. & Wilkinson, A. J. The effect of crystal orientation on the indentation response of commercially pure titanium: experiments and simulations. *Proc. R. Soc. A* **466**, 695–719 (2010).
46. Britton, T. B. & Wilkinson, A. J. High resolution electron backscatter diffraction measurements of elastic strain variations in the presence of larger lattice rotations. *Ultramicroscopy* **114**, 82–95 (2012).
47. Ulvestad, A., Clark, J. N., Harder, R., Robinson, I. K. & Shpyrko, O. G. 3D imaging of twin domain defects in gold nanoparticles. *Nano Lett.* **15**, 4066–4070 (2015).
48. Yau, A., Cha, W., Kanan, M. W., Stephenson, G. B. & Ulvestad, A. Bragg coherent diffractive imaging of single-grain defect dynamics in polycrystalline films. *Science* **356**, 739–742 (2017).
49. Yu, H., Liu, J., Karamched, P., Wilkinson, A. J. & Hofmann, F. Mapping the full lattice strain tensor of a single dislocation by high angular resolution transmission Kikuchi diffraction (HR-TKD). *Scr. Mater.* **164**, 36–41 (2019).
50. Wallis, D., Hansen, L. N., Britton, T. B. & Wilkinson, A. J. High-angular resolution electron backscatter diffraction as a new tool for mapping lattice distortion in geological minerals. *J. Geophys. Res. Solid Earth* **124**, 6337–6358 (2019).
51. Humphreys, F. J. Grain and subgrain characterisation by electron backscatter diffraction. *J. Mater. Sci.* **36**, 3833–3854 (2001).

Methods

Materials. Nafion 117, Nafion 520D dispersion, platinum black, Sigracet 35BC and Sigracet 39BC were purchased from Fuel Cell Store. Sodium perchlorate, sodium citrate tribasic dihydrate (>99.0%), Au foil, Au wire (>99.99+%) and gold(III) chloride trihydrate ($HAuCl_4$, 99.9%) were purchased from Sigma-Aldrich. Isopropanol (high-performance liquid chromatography grade) and HCl (certified American Chemical Society Plus) were purchased from Fischer Scientific. Ag/AgCl reference electrodes filled with 3.0 M KCl were purchased from World Precision Instruments. LF-2 leakless Ag/AgCl reference electrodes were purchased from Warner Instruments. The 4932 ppm H_2, 520 ppm CO, N_2 (99.99%) and CO_2 (99.99%) gases were purchased from Praxair.

Sample and electrode preparation. Au nanoneedles on carbon fibre electrodes were prepared by a modified electrodeposition method. A single-compartment electrochemical cell was filled with 0.5 M HCl and 0.09 M $HAuCl_4$ electrolyte. A Au foil counter electrode and a Ag/AgCl reference electrode were used. A thin layer of Au was deposited by subjecting the hydrophobic side of a Sigracet 39BC electrode to a pulse electrodeposition protocol (0.03 s at −0.4 V versus Ag/AgCl, followed by 2 s at open circuit potential) for 400 cycles[52,53]. Additional Au dendrite growth was induced by holding the working electrode at −0.4 V versus Ag/AgCl for 300 s. The electrode was then thoroughly rinsed with deionized water. The total surface area of the electrode was determined after electrolysis to be 8.8 cm^2 via the gold-oxide stripping method, corresponding to a roughness factor of 11.7 (ref. [54]).

Pt on C membrane–electrode assembly anodes were prepared by drop drying a 2.5 mg ml^{-1} solution of Pt black in isopropanol with 0.08 wt% Nafion 520D onto Sigracet 35BC. The mass loading of each electrode was approximately 660 μg cm^{-2}. Nafion 117 was hot-pressed onto the Pt/C electrode by compressing the electrode at 2,000 psi for 90 s between two Teflon-lined brass plates held at 130 °C.

Au nuggets (Samples A and B) were prepared from Au wire (>99.99%) with a diameter of 0.5 mm. The wire was melted with a butane torch (RS Components), resulting in a small Au sphere (diameter of 1–1.5 mm) at the end of the wire, and quenched in cooled deionized water (18.2 MΩ cm; <10 °C). The Au sphere was then gently compressed with atomically flat Si wafers (Inseto) attached to a custom-made toolmaker vice. The flattened Au nuggets were subsequently annealed at ~900 °C and slowly cooled in air. The prepared Au nuggets were characterized with EBSD using a field emission SEM instrument (JSM-7800F, JEOL) equipped with Symmetry electron backscatter detectors and running the Oxford Aztec software in order to identify the crystal indices of the individual grains. The flattened area on the Au nugget was typically 1–2 mm^2 and typically contained between 15 and 20 grains with different crystal indices. Prior to SECCM experiments, the Au nugget was placed in a furnace at 270 °C for 80 minutes and cooled in air.

Gas diffusion electrolyses in citrate electrolyte. A CH Instruments 660D potentiostat was used for gas diffusion electrolysis measurements. An LF-2 Ag/AgCl electrode and a Pt/C Nafion membrane–electrode assembly were used as the reference and counter electrodes, respectively. The cathode consisted of an Au layer electrodeposited onto Sigracet 39BC (preparation described above). A 370 μl custom electrochemical cell (described in depth elsewhere)[28] with a 0.75 cm^2 electrode contact area was filled with 10 mM sodium citrate and 490 mM $NaClO_4$ (pH, 5.5). CO_2 flow into the cell was set at 10 sccm using an Alicat mass flow controller, while a New Era 1000 syringe pump was used to flow electrolyte into the cell at 150 μl min^{-1}. Potentiostatic electrolyses (~550 s each) were conducted by stepping the potential in −100 mV increments from −0.8 to −1.1 V versus Ag/AgCl.

The product stream directly flowed into the sampling loop of a gas chromatograph (SRI Instruments) equipped with a packed MolSieve 13X column and a packed HaySep D column. The amount of CO and H_2 (the only products) produced were quantified by comparing the chromatograph peak integral to standard calibration gas mixtures. Molar amounts were converted to charge to obtain faradaic efficiency.

Nanopipette preparation and SECCM procedure. Nanopipettes were fabricated from borosilicate capillaries (GC120F-10, Harvard Apparatus; capillary dimensions: outer diameter, 1.2 mm; inner diameter, 0.69 mm; length, 100 mm) with a CO_2-laser puller (Sutter Instruments P-2000; pulling parameters, line 1 with HEAT 330, FIL 3, VEL 30, DEL 220 and PUL−; and line 2 with HEAT 330, FIL 3, VEL 40, DEL 180 and PUL 120). The nanopipettes possessed a tip opening of ~200 nm, characterized with field emission SEM (GeminiSEM 500 system, Zeiss); a representative SEM image can be found in Supplementary Fig. 1. The nanopipette was filled with 10 mM citrate buffer (pH, 5.5), equipped with a QRCE (AgCl-coated Ag wire) and mounted on a *z*-piezoelectric stage (P-753.2 LISA, Physik Instrumente) with a custom-made pipette holder. A thin layer of silicone oil was added on top to minimize electrolyte evaporation during the experiment[27]. The QRCE was calibrated routinely (for example, before and after the SECCM measurements) in 10 mM citrate solution (pH, 5.5) with respect to a commercial leakless Ag/AgCl electrode (3.4 M KCl, ET072, eDAQ), resulting in a stable potential of +184 ± 3 mV. Initial attempts to use 10 mM $KHCO_3$ electrolyte with pH = 8 led to droplet instability after collecting more than 150–180 pixels in SECCM. By contrast, the 10 mM citrate, pH = 5.5 electrolyte allowed for long-term stability and the collection of 1,000 s of pixels. All electrochemical results in this work are presented versus Ag/AgCl (3.4 M KCl).

A prepared Au nugget sample was glued onto a standard SEM pin stub (diameter, 12.5 mm; Agar) with conductive Ag paint (RS Components) and fixed at the centre of a homemade environmental cell[23]. The sample was then electrically connected to an external (home-built) electrometer head using a copper wire. The environmental cell was manufactured by modifying a commercially available airtight polypropylene container (Lock & Lock). A part of the container lid was cut and sealed with standard cover glasses, enabling visualization of the Au surface with a high-resolution optical camera (Pixelink; CompactTL ×8 telecentric lens, Edmund Optics). A two-way Omnifit connector (Kinesis), drilled in and fixed in place with epoxy resin (Sigma-Aldrich) at the side of the cell, served as a CO_2 or Ar inlet port. The gas was humidified with a threaded midget bubbler (Sigma-Aldrich) and supplied into the environmental cell with a consistent flow of 80 ml min^{-1}. The entire environmental cell was fixed onto a sample holder, which was mounted on an *xy*-piezoelectric stage (P-733.2 XY, Physik Instrumente). The nanopipette was positioned above the surface of interest using *xyz* micropositioners (M-461-XYZ-M, Newport) and translated close to the Au surface with a stepper motor (8303 Picomotor Actuator, Newport). All instruments for tip positioning and current amplification were placed on a vibration isolator (BM-8, Minus K) and encapsulated within a Faraday cage, which was equipped with vacuum-sealed panels (Kevothermal) and aluminium heat sinks, in order to minimize electrical and mechanical noise and maintain thermal equilibrium during SECCM scanning.

The QRCE potential was controlled with respect to ground, and the current flowing at the Au working electrode (i_{surf}, held at a common ground) was measured using a home-built current amplifier at a bandwidth of 5 kHz. The i_{surf} was measured every 4 μs, and these data averaged 512 times to result in a data acquisition rate of 2.052 ms (0.004 × (512 + 1) = 2.052 ms, where one extra iteration is used to transfer the data to the host computer). In rare cases during an SECCM scan (<1% of the pixels), electronic noise results in the droplet missing contact with the surface during a hop. These pixels are represented as the average of adjacent pixels in an SECCM image, but are not included in the reported statistics in the histograms or in Supplementary Table 2. Data acquisition and instrumental control was carried out using a field programmable gate array (FPGA) card (PCIe-7852R, National Instruments) controlled by a LabVIEW 2016 (National Instruments) interface running the Warwick Electrochemical Scanning Probe Microscopy (http://www.warwick.ac.uk/electrochemistry/wec-spm) software.

Voltammetric SECCM with a hopping scanning mode was utilized herein[25,55]. At each position (that is, pixel in maps), the nanopipette initially approached the surface at the applied potential (E_{app}, calibrated to the commercial leakless Ag/AgCl electrode) of 0.92 V until the meniscus at the end of the nanopipette tip contacted the Au surface, satisfying a threshold of 1.21 pA in i_{surf}. Subsequently, E_{app} was switched to −0.33 V and held for 0.1 s, prior to measuring a LSV at a scan rate of 0.5 V s^{-1} for CO_2 electroreduction or the hydrogen evolution reaction. Once the LSV measurement was complete, the nanopipette was retracted from the surface before proceeding to the next pixel. Overall, the entire procedure resulted in a pixel acquisition time of around 2.5 s $pixel^{-1}$. Typical scanning time ranged from 15 to 55 minutes (that is, for 369 to 1,281 pixels, respectively). Each individual pixel constituted an LSV carried out over a potential range of −0.33 V to −1.08 V, which could be represented as over 730 equipotential images (1 mV separation between images) in a single scan.

SEM imaging and HR-EBSD strain mapping. SEM and EBSD images were acquired with a TFS Apreo S SEM system equipped with a Bruker Quantax EBSD 400i system or a Zeiss SUPRA field emission SEM system equipped with a Nordlys EBSD detector (Oxford Instruments). HR-EBSD data were collected using a TFS Apreo S SEM system equipped with a Bruker Quantax EBSD 400i system. The sample stage was tilted 70° during acquisition. HR-EBSD patterns were collected using a pattern resolution of 1,600 × 1,200, exposure time of 80 ms and 2 × 2 binning. HR-EBSD maps were collected at ×2,500 magnification and a step size of ~170 nm. Cross-correlation and strain analysis was performed with CrossCourt 3.2 from BLG Productions, correcting for beam position effects with an effective camera pixel size of 37.5 μm. Pattern analysis was performed using 74 256 × 256 regions of interest designated within the patterns. Filtering in the Fourier domain was performed with the following settings: high frequency cut-off, 39; high frequency width, 36; low frequency cut-off, 2; and low frequency width, 1. All HR-EBSD data are referenced to a pixel distal to the GB of interest. Strains reported correspond to the normal strains in the *x*, *y* and *z* directions.

Data availability

The authors declare that all data supporting the findings of this study are included within the paper and its Supplementary Information files. Source data are available from the corresponding authors upon reasonable request.

References

52. Liu, M. et al. Enhanced electrocatalytic CO_2 reduction via field-induced reagent concentration. *Nature* **537**, 382–386 (2016).
53. Wang, Y. & Hall, A. S. Pulsed electrodeposition of metastable $Pd_{31}Bi_{12}$ nanoparticles for oxygen reduction electrocatalysis. *ACS Energy Lett.* **5**, 17–22 (2020).
54. Hamelin, A. Cyclic voltammetry at gold single-crystal surfaces. Part 1. Behaviour at low-index faces. *J. Electroanal. Chem.* **407**, 1–11 (1996).
55. Chen, C.-H. et al. Voltammetric scanning electrochemical cell microscopy: dynamic imaging of hydrazine electro-oxidation on platinum electrodes. *Anal. Chem.* **87**, 5782–5789 (2015).

Acknowledgements

Work at Stanford was supported by the National Science Foundation (CHE-1855950). R.G.M. gratefully acknowledges Stanford University for a DARE fellowship and J.A.R. gratefully acknowledges a Stanford Graduate Fellowship. M.K. and P.R.U. are grateful to the Warwick–Monash Accelerator Fund for support. M.K. also acknowledges support from the Leverhulme Trust for an Early Career Fellowship. I.J.M. and P.R.U. are supported by Engineering and Physical Sciences Research Council Programme Grant EP/R018820/1. P.R.U. thanks the Royal Society for a Wolfson Research Merit Award. O.J.W. acknowledges support from the University of Warwick Chancellor's International Scholarship. Parts of this work were performed at the Stanford Nano Shared Facilities, which is supported by the National Science Foundation under award ECCS-1542152.

Author contributions

R.G.M., M.K., P.R.U. and M.W.K. conceived and designed the study. R.G.M., M.K. and O.J.W. performed SECCM experiments. O.J.W. prepared Au samples for SECCM imaging. R.G.M. and J.A.R. performed gas diffusion electrode electrolysis studies. R.G.M., M.K. and O.J.W. performed SEM/EBSD imaging of the samples, and R.G.M. performed HR-EBSD measurements and analysis. I.J.M. and P.R.U. designed the finite element method calculations, and I.J.M. built the COMSOL model. R.G.M., M.K. and M.W.K. wrote the initial draft of the paper, and all authors contributed to the final version.

Competing interests

The authors declare no competing interests.

Additional information

Supplementary information The online version contains supplementary material available at https://doi.org/10.1038/s41563-021-00958-9.

Correspondence and requests for materials should be addressed to P.R.U. or M.W.K.

Peer review information *Nature Materials* thanks the anonymous reviewers for their contribution to the peer review of this work.

Reprints and permissions information is available at www.nature.com/reprints.